Design and control of a bio-inspired soft wearable robotic device for ankle–foot rehabilitation

Yong-Lae Park[1], Bor-rong Chen[2], Néstor O Pérez-Arancibia[3],
Diana Young[4,5], Leia Stirling[6], Robert J Wood[4,5], Eugene C Goldfield[5,7]
and Radhika Nagpal[4,5]

[1] Robotics Institute, Carnegie Mellon University, Pittsburgh, PA 15213, USA
[2] BioSensics, LLC., Cambridge, MA 02142, USA
[3] Department of Aerospace and Mechanical Engineering , University of Southern California,
Los Angeles, CA 90089, USA
[4] School of Engineering and Applied Sciences, Harvard University, Cambridge, MA 02138, USA
[5] Wyss Institute for Biologically Inspired Engineering, Harvard University, Boston, MA 02115, USA
[6] Department of Aeronautics and Astronautics, Massachusetts Institute of Technology, Cambridge,
MA 02139, USA
[7] Boston Children's Hospital, Boston, MA 02115, USA

E-mail: ylpark@cs.cmu.edu

Abstract

We describe the design and control of a wearable robotic device powered by pneumatic artificial muscle actuators for use in ankle–foot rehabilitation. The design is inspired by the biological musculoskeletal system of the human foot and lower leg, mimicking the morphology and the functionality of the biological muscle–tendon–ligament structure. A key feature of the device is its soft structure that provides active assistance without restricting natural degrees of freedom at the ankle joint. Four pneumatic artificial muscles assist dorsiflexion and plantarflexion as well as inversion and eversion. The prototype is also equipped with various embedded sensors for gait pattern analysis. For the subject tested, the prototype is capable of generating an ankle range of motion of 27° (14° dorsiflexion and 13° plantarflexion). The controllability of the system is experimentally demonstrated using a linear time-invariant (LTI) controller. The controller is found using an identified LTI model of the system, resulting from the interaction of the soft orthotic device with a human leg, and model-based classical control design techniques. The suitability of the proposed control strategy is demonstrated with several angle-reference following experiments.

Keywords: soft robotics, bio-inspired robotics, wearable robotics, active orthosis, pneumatic artificial muscles (PAMs), soft sensors, feedback control

(Some figures may appear in colour only in the online journal)

1. Introduction

Ankle–foot pathologies in patients with neuromuscular disorders, caused by cerebral palsy (CP), amyotrophic lateral sclerosis, multiple sclerosis, or stoke, can result in abnormal gaits over time, such as drop foot, equinus, and crouch gait [1]. The treatment of these pathologies using active orthotics has the potential not only for providing immediate assistance during gait but also for preventing the development of abnormal gaits over time.

In this paper, we present an active soft orthotic device—incorporating sensing, control, and actuation—for use in treating ankle–foot pathologies associated with neuromuscular disorders [2]. The design mimics the muscle–tendon–ligament–skin architecture in the biological
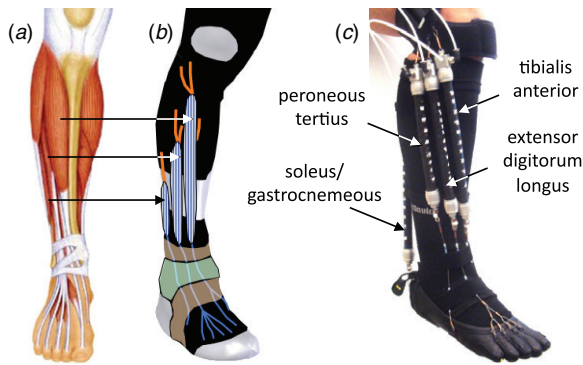
Figure 1. Design and prototype of bio-inspired active soft orthotic device. (*a*) Lower leg muscle anatomy. (*b*) Design concept. (*c*) Actual prototype.

musculoskeletal system of the human ankle, as shown in figure 1.

There have been various approaches for treating ankle–foot pathologies. One of the most typical solutions is to wear rigid (or semi-rigid) ankle braces, such ankle–foot orthoses (AFOs) [3–6]. These devices improve gait abnormalities by forcing the ankle joint angle to be close to 90°. However, long-term use of these passive devices causes disuse atrophy of muscles and consequently makes the user physically dependent on the device [7, 8]. Furthermore, long-term use of passive AFOs may induce neural adaptations with gradual reduction of muscle activity over time [9]. For example, previous work shows neural adaptation of motor representation occurs with spinal cord injury or immobilization [10, 11]. Thus, passive AFOs can increase the time needed in physical therapy to compensate for these unwanted long-term effects.

Active devices are another approach to address pathological gaits. While active devices require relatively complicated systems compared to passive braces, with appropriate control, they not only can provide higher independence, as shown with robotic prosthetic legs [12, 13], but also can be used for re-educating the neuro-motor system [14], with previous work showing the efficacy of adaptive control with active devices [15]. In addition, robotic gait training and rehabilitation has demonstrated benefits on improving abnormal gaits associated with neuromuscular disorders [16, 17]. Several actuation methods have been employed to obtain active elements. For example, brushless dc motors have been used for an ankle rehabilitation robot [18], as well as in series elastic actuators with a rigid plastic AFO frame [15, 19]. Powered AFOs have been proposed for supplementing weak muscles for both dorsiflexion and plantarflexion using McKibben pneumatic artificial muscle actuators [20, 21] and bidirectional pneumatic rotary actuators [22], combined with carbon fiber reinforced foot and leg frames. In [23], a robotic tendon using a spring-based linear actuator has been proposed to provide active gait assistance. Active orthotic devices using magnetorheological fluid [24] and electrorheological fluid [25] have been developed to provide variable damping characteristics. However, the devices mentioned above all require rigid frames and linkages and mechanical joints, which reduce the number of natural

degrees of freedom of the joint. To avoid limiting the motion of the joint, the applicability of using shape memory alloy (SMA) wire springs has been investigated to create a prototype soft actuated knee brace [26]. Although SMA wires showed potential to be embedded in a flexible structure, achieving appropriate power management and response time presented strong challenges for developing a practical orthotic device. Soft wearable devices using cable-driven actuation [27] and pneumatic muscle actuation [28] have shown similar concepts to the proposed system in this paper. However, they were targeted to upper extremity rehabilitation.

In contrast to prior orthotic designs that either constrain or actuate the ankle joint only in the sagittal plane, the device presented in this paper (figure 2) has multiple artificial muscle–tendon units that mimic not only the morphology but also the functionality of the biological muscles in terms of its ability to control varied sagittal and mediolateral ankle motions such as dorsiflexion, plantarflexion, inversion, and eversion. In addition to this biomimetic design, the device uses soft sensors, actuators, and structures that do not constrain the user's natural degrees of freedom, which is not possible in traditional exoskeleton robots. The prototype is made of soft plastics and composite materials that comprise a light and flexible, but robust structure. The device is also equipped with various sensors, including strain sensors, inertial measurement units (IMUs), and pressure sensors. The strain sensor and the IMUs provide information on joint angle, while the pressure sensors detect foot contact with the ground. In order to demonstrate the suitability of the proposed approach, we present experimental results by showing the characterization of the individual components, as well as demonstrate controllability of the device using a linear time-invariant (LTI) controller in several angle-reference following experiments. Ultimately, we envision a system that not only can increase the efficiency of rehabilitation by enhancing muscle usage but can also potentially provide assistance during gait by increasing safety and stability.

The rest of the paper is organized as follows. Section 2 describes the design and fabrication of the prototype. Section 3 discusses the sensor validation and mechanical characterization of the system. Section 4 presents the control strategy and experimental cases. We conclude with a discussion of future work, which includes potential extensions of the prototype.

2. Design

The basic design concept was to create an external artificial muscle–tendon–ligament structure by mimicking the existing biological musculoskeletal system, as described in figure 1. This concept allows us to achieve three design requirements: no rigid frame structures, no constraints on the natural joint motions, and non-invasiveness. The prototype is composed of three physical layers: base, actuation, and sensing. The control hardware connects the actuation and sensing layers to enable the execution of complex control rules. The entire prototype, including electronics and batteries but not including the mass of the air source, weighs approximately 950 g.
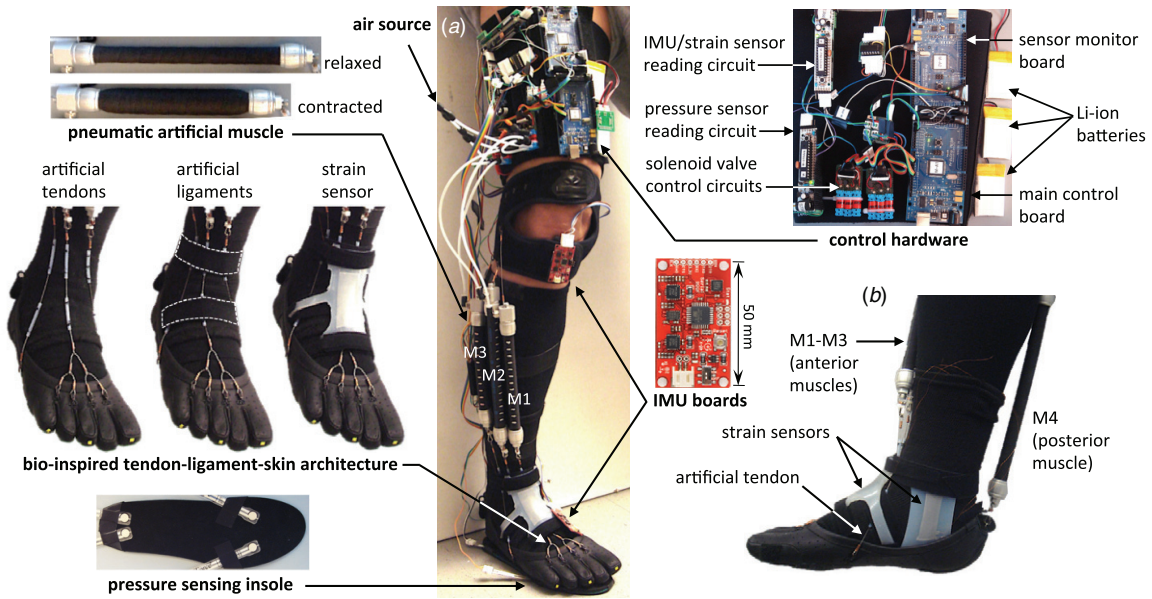
Figure 2. Main design of the active soft orthotic device (highlighting key components). (*a*) Front view of the prototype integrated on a human leg showing the three anterior muscles (M1: tibialis anterior, M2: extensor digitorum longus, and M3: peroneous tertius). (*b*) Side view of the prototype showing the posterior muscle (M4: gastrocnemius) and the strain sensors.

2.1. Base

The base layer contains the foot, ankle, and knee braces that make physical contacts with the wearer's skin. Through this layer, the actuation forces are transmitted to the human body. A flexible commercial knee strap (419 Multi-Action Knee Strap, McDavid, Woodridge, IL 60517, USA), an ankle brace (511 Elastic Ankle Support, McDavid, Woodridge, IL 60517, USA), and a leather shoe (Performa, Vibram, Albizzate, Italy), with no rigid components, were modified to be used as the knee, ankle, and foot braces, respectively.

2.2. Actuation

The actuation layer is composed of artificial muscles, tendons, and ligaments. Four artificial muscles were placed on the lower leg (three anterior muscles for dorsiflexion, inversion, and eversion, as well as one posterior muscle for plantarflexion), with their artificial tendons anchored at the knee brace and the foot brace. The artificial muscles were designed as counterparts to the biological muscles for dorsiflexion, plantarflexion, inversion, and eversion, respectively, so that the device could provide the supplementary forces to the corresponding muscles. The artificial tendons were placed close to where the corresponding biological tendons were located. As the artificial muscles contract, their artificial tendons pull the anchors on the foot brace, resulting in a corresponding ankle motion. To prevent the knee brace from slipping during actuation, thin non-slip silicone pads were firmly fixed at the inside of the knee brace making physical contacts to the wearer's skin. Since the four artificial muscles can be actuated independently, they can generate active mediolateral motions, such as inversion and eversion, as well as active sagittal motions, such as dorsiflexion and plantarflexion. These mediolateral motions will be useful for

foot stability control during the ground contact phase of walking.

The actual prototype worn on a subject's right leg is shown in figure 2. Four off-the-shelf pneumatic artificial muscles (DMSP-10-120-200, 180, 160, and 140, Festo, Esslingen, Germany) were used for actuation, and two off-the-shelf miniature solenoid valves (NEX-2-03-L, Parker Hannifin Corp., Cleveland, OH 44124, USA) were installed for air injection and release of each muscle. The proximal side of each muscle was anchored to the knee brace, and the distal side was anchored to the foot brace through metal tendon cables that are flexible but inextensible. Metal hooks were firmly sewn onto the multiple places of the knee and foot braces to provide anchoring points for the tendon cables. The hooks made the muscles easy to attach to and detach from the braces. Since the knee brace has anchoring points only below the knee joint, the device does not constrain the knee range of motion. Muscles 1 and 3 (mimicking the tibialis anterior and peroneus tertius, respectively) provide inversion and eversion functions, respectively, as well as active dorsiflexion, while muscle 2 (mimicking the extensor digitorum longus) provides only dorsiflexion. Muscle 4 (mimicking gastrocnemious) provides active plantarflexion. Figure 3 shows possible active ankle motions generated by different combinations of actuated muscles. This agonist–antagonist muscle architecture not only can create desired ankle motions but also can provide physical support by increasing the stiffness of the ankle joint with co-contraction.

Figure 2(*a*) shows the tendon system. While muscles 1, 3, and 4 each have only one anchor on the distal side, muscle 2 has multiple anchors on the foot brace. The differential tendon mechanism of muscle 2, similar to the foot design of a wall-climbing robot [29], distributes the pulling force from one tendon cable to four anchors. Flexible Teflon® tubes, sewn onto the foot brace, secure the paths of force transmission
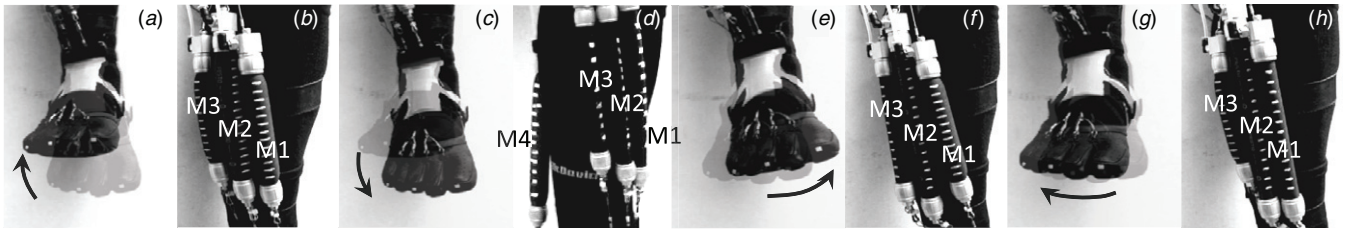
Figure 3. Actively assisted ankle motions: (*a*) dorsiflexion (*b*) with all three anterior muscles contracted; (*c*) plantarflexion (*d*) with only muscle 4 contracted; (*e*) inversion (*f*) with only muscle 1 contracted; (*g*) eversion (*h*) with only muscle 3 contracted.
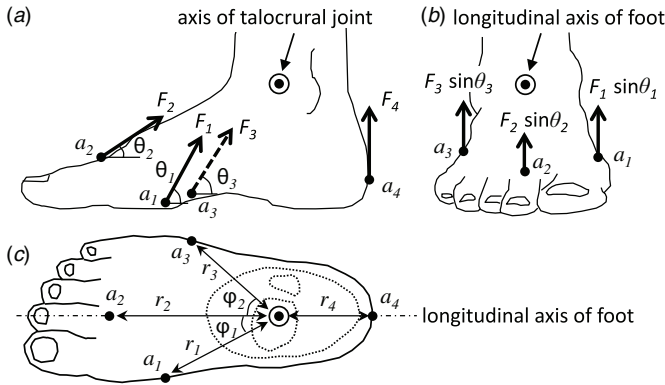
Figure 4. Actuation system configuration and its parameters (*a_i*: anchor location of tendon *i*, *F_i*: contraction force of muscle *i* connected to tendon *i*, *θ_i*: vertical angle of tendon *i*, and *φ_i*: horizontal angle of tendon *i*.). (*a*) Side view of foot to show sagittal motions. (*b*) Front view of foot to show mediolateral motions. (*c*) Top view of foot.

Figure 5. (*a*) Strain sensor prototype with dimensions. (*b*) Prototype in action showing resistance change with strain (unit: Ω).

by allowing the cables to smoothly slide through with muscle actuation. In addition to the teflon tubes, the artificial ligaments made of nylon straps were added to constrain the lateral motions of the cables while allowing only axial motions.

Figure 4 shows how the actuation system of the prototype applies torques to the ankle based on the foot and ankle models in [6]. Dorsiflexion is achieved by the cooperation of three anterior muscles, and plantarflexion by the posterior muscle. Assuming the force directions at the tendon anchors are perpendicular to the sagittal plane, their torques can be calculated as

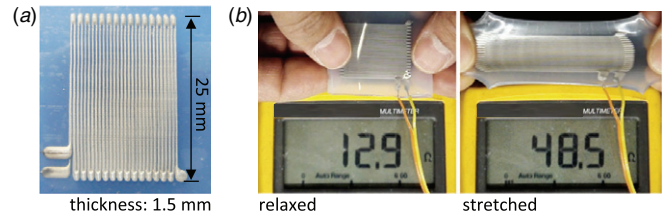$$\tau_{\text{dorsi}} = F_1 r_1 \sin\theta_1 \cos\phi_1 + F_2 r_2 \sin\theta_2 + F_3 r_3 \sin\theta_3 \cos\phi_2,$$
(1)

$$\tau_{\text{plantar}} = F_4 r_4.$$
(2)

In the same way, the torques for mediolateral motions are

$$\tau_{\text{inversion}} = F_1 r_1 \sin\theta_1 \sin\phi_1,$$
(3)

$$\tau_{\text{eversion}} = F_3 r_3 \sin\theta_3 \sin\phi_2.$$
(4)

Based on the configurations of the artificial tendons and the dimensions of the prototype, the maximum torques the system can apply are 110 Nm, 53 Nm, 20 Nm, and 21 Nm for dorsiflexion, plantarflexion, inversion, and eversion, respectively.

2.3. Sensing

The sensors are the outermost layer of the prototype and are composed of three sensing modalities. We are interested in information about the configuration of the leg and how the user is interacting with the ground. Thus we focus on strain, inertial, and pressure sensors.

2.3.1. Strain sensor. Two custom-built strain sensors were used for measuring the ankle joint angles, as shown in figure 2(*b*). One was attached on the dorsal side of the ankle for measuring sagittal angle changes, and the other was placed on the medial side for detecting mediolateral motions. Although there are different types of commercial strain gauges, none of them are designed for accurately measuring large strain on a flexible surface. Figure 5 shows the design and the actual prototype of the custom-built strain sensors. Microchannels, filled with a liquid metal alloy, Eutectic Gallium–Indium (EGaIn), were embedded in a silicone elastomer (EcoFlex0030, Smooth-On, Inc., Easton, PA 18042, USA) sheet, as described in [30]. When the material experiences axial strain, the overall channel length increases and the cross-sectional areas of the channels decrease resulting in increased electrical resistance of the microchannel. Since the microchannels are filled with liquid, the strain sensor is highly flexible and stretchable. The channel size is 250 μm × 250 μm, and the overall thickness of the sensor is 1.5 mm. The nominal resistance at rest is 10.3 Ω. The experimental gauge factor of the strain sensor is 3.4. The gauge factor did not show any noticeable difference with a relatively mild temperature change (between 20 and 40 °C), which was acceptable for an indoor rehabilitation device as its current form. However, a thorough investigation on the performance with more extreme temperature changes is one of our on-going research areas to make the device more mobile and assistive in the future. More details on this strain sensor, such as design, fabrication, and calibration, can be found in [31, 32].

2.3.2. Inertial measurement unit. Two off-the-shelf 9-degree-of-freedom IMUs (SEN-09623, 9DOF Razor IMU, Sparkfun Electronics, Boulder, CO 80301, USA) were used for measuring the orientations of the lower leg and the foot. These IMUs provide sensor data from three different types of microelectromechanical systems based sensors: 3D accelerometer, 3D angular rate gyroscope, and low-field 3D magnetometer. An on-chip sensor fusion algorithm, provided by the manufacturer of the IMU boards, derives the 3D orientation of each IMU using the sensor inputs. From the two IMUs, one mounted on the foot and the other on the lower leg, the ankle joint angles, as Euler angles, can be computed by calculating the rotation matrices, as described in [33].

While it is possible to measure joint angles using only IMUs (using two per joint), joint angle measurement using the strain sensor, with inertial measurement employed only for initial calibration, offers the significant advantage of lower power consumption. IMU subcomponents, specifically the gyroscopes that enable angle estimation, require higher power consumption than the strain sensor. In this implementation, a single strain sensor consumes approximately 0.625 mW of power, while the accelerometers and gyroscopes included in just one of the IMUs in this design consume approximately 36 mW. Future implementations of this sensor system may enable power savings by including only one IMU to provide absolute angle reference, as well as sleeping the IMU after initial strain sensor calibration. Reducing the number of IMUs required for joint angle measurement in favor of the strain sensing method also provides design advantages, as the strain sensors may be more easily and comfortably embedded within soft architectures.

2.3.3. Pressure sensor. Foot pressure sensing is required to identify ground contact events. While the strain sensors and IMUs measure the ankle joint angle, the foot pressure sensors detect relative pressure distribution on the foot from ground contact. The pressure sensors determine which part of the foot was in contact with the ground in real time. Four off-the-shelf force sensitive resistors (FSRs) (FlexiForce-A201-25lb, Tekscan Inc., Boston, MA 02127, USA) were embedded in a shoe insole. Although the pressure sensors are currently used as on–off switches, they can also be used to measure actual foot pressures with accurate calibration if necessary.

2.4. Control hardware

The control hardware (electronics), including batteries, were attached to a modified thigh brace (473 Thigh Sleeve, McDavid, Woodridge, IL 60517, USA), containing multiple micro-controller units (MCUs) to support tasks divided into four major stages: sensing, signal processing, control, and actuation.

The sensing stage samples all the sensors, including strain sensors, IMUs, and a pressure sensor, at 50 Hz using independent MCUs (Atmega328P, Atmel, San Jose, CA 95131, USA). The signal processing stage applies a different algorithm to each sensor type to process different types of sensor data. Then, the control stage runs a control loop at
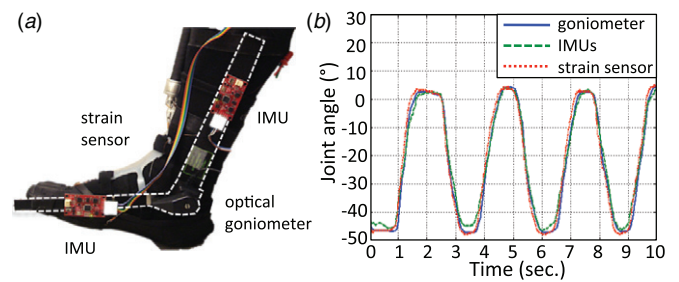
Figure 6. Sensor validation experiments. (*a*) Experimental setup with a strain sensor, two IMUs, and a goniometer. (*b*) Sensor validation result with ankle joint angle measurement. More details on this characterization can be found in [2].

50 Hz for actuation by accessing all the sensor data using its own MCU (Atmega1280, Atmel, San Jose, CA 95131, USA). Finally, the actuation stage carries out control commands generated at the previous stage by controlling solenoid valves through pulse-width-modulation (PWM). More details on the control hardware can be found in [2].

3. Characterization

The prototype was characterized in two functional categories, sensing and actuation, to understand how the device performs given the non-rigid nature of all of the components. Power consumption is also briefly discussed at the end of this section. All the testing was done with one human subject, and the testing procedure was reviewed by the Harvard Medical School Committee on Human Studies.

3.1. Sensor validation

Three types of sensing were characterized: sagittal angle sensing, mediolateral angle sensing, and foot pressure sensing.

3.1.1. Sagittal joint angle sensing. For joint angle measurement, the dorsal strain sensor was selected as a reliable source of angle information during operation. However, since the strain sensor requires calibration, each time a user wears the device, due to the change of the sensor location, the IMUs are used for calibrating the strain sensor by establishing a linear mapping between the strain sensor readings and joint angles measured by the IMUs. The performance of the strain sensor and the IMUs were evaluated using a commercial optical goniometer (PASPORT Goniometer Sensor PS-2137, PASCO, Roseville, CA 95747, USA).

A validation experiment was conducted to examine the performance of the dorsal strain sensor and the IMUs with the goniometer used as ground truth. The two IMUs were attached to the goniometer, and the goniometer was mounted to the interior part of the subject's right foot. The strain sensor was attached to the anterior part of the ankle, as shown in figure 6(*a*). Once all the sensors were mounted, the subject freely moved the ankle in plantarflexion and dorsiflexion for 20 min. A representative 10 s segment from the experiment is shown in figure 6(*b*). The result showed that both the strain sensor and IMUs provided accurate joint angle
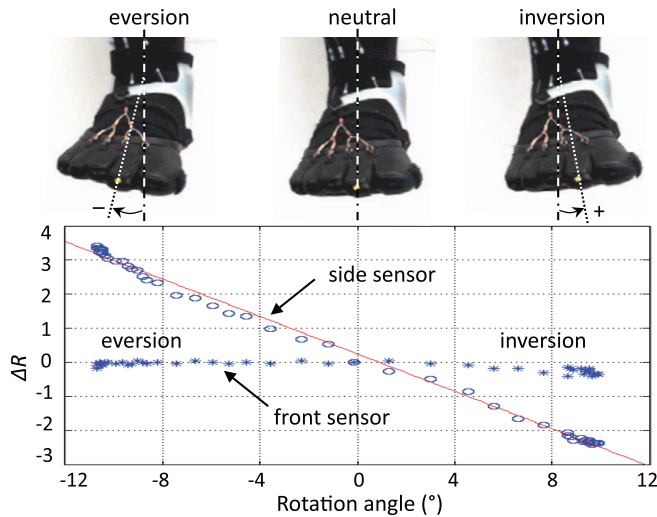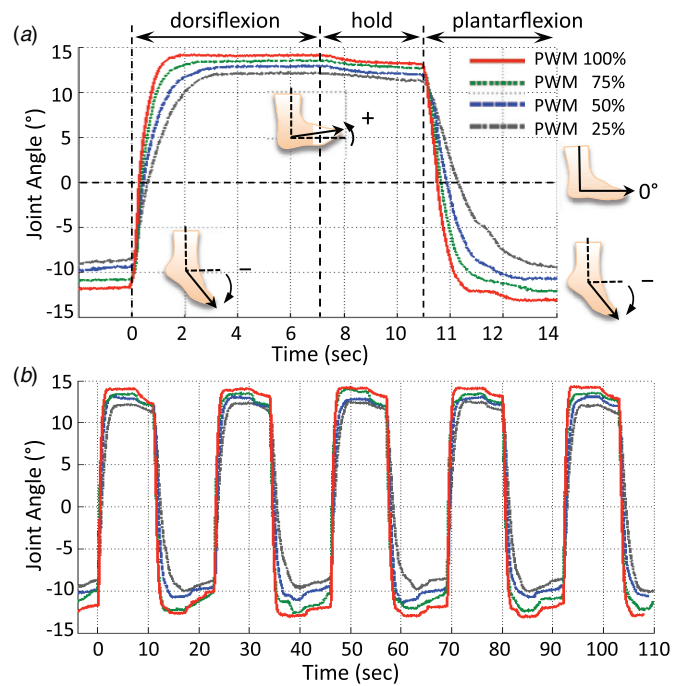
Figure 7. Mediolateral ankle motions and strain sensor calibration result.

Figure 8. Mechanical characterization results. (*a*) Maximum dorsiflexion and plantarflexion with various PWM duty cycles. (*b*) Repeated sagittal ankle motions with the PWM duty cycles shown in (*a*).

measurements during the experiment. The mean error of the IMU measurement was $0.1° \pm 2.9°$, with a maximum error of $9.1°$. The mean error of the strain-derived angle was $0.3° \pm 1.6°$, with a maximum error of $4.3°$.

The strain sensor experienced approximately 73% strain during full dorsiflexion and plantarflexion tests. To fully utilize the calibration region (0–100% strain), the sensor was stretched with 20% pre-strain and installed from a full dorsiflexion position. Also, the two ends of the sensor were firmly attached to the ankle brace with non-stretchable nylon straps to minimize any possible sliding effect, a potential error source, between the sensor and the ankle brace. This type of strain sensor requires approximately 3N of tensile load for 100% strain according to [34], which is negligible compared to the contraction force of the pneumatic muscles.

3.1.2. Mediolateral joint angle sensing. In addition to sagittal motions, mediolateral motions were characterized (figure 7) using a pre-stretched strain sensor placed at the side of the ankle. Two anterior muscles, M1 and M3, were actuated alternately creating inversion and eversion motions while the other two muscles, M2 and M4, were fully relaxed, and the strain sensor signal was measured. Since the goniometer was not able to measure these rotational angles, we used professional video analysis software (ProAnalyst, Xcitex, Cambridge, MA 02141, USA) to provide reference angles. The result showed a linear sensor response for measuring mediolateral ankle angles.

3.1.3. Foot pressure sensing. The FSR pressure sensors were characterized in order to determine the threshold for detecting the ground contact of the foot. With no load, the resistance of the pressure sensors was at or above 1 MΩ. With a 143 lb adult standing on the insole, the resistance was consistently less than 500 kΩ. Thus, 500 kΩ was selected as the threshold for the subject tested. This threshold value is easily tunable for different users.

3.2. Actuation system characterization

The mechanical system was characterized to evaluate the response time, linearity, and repeatability of the actuation system. The prototype was installed in the subject's right leg (figure 2). The subject sat on a rigid bench hanging the foot in the air and was able to move the leg and the foot without any constraint.

Due to the nonlinearity of pneumatic muscles, proportional control of the actuators was not as straightforward as for other linear actuators, such as dc motors. One method for proportional control is to use proportional valves that control the input air pressure of the muscles by changing input voltage [35]. Another method is PWM control of binary on/off solenoid valves [36, 37]. In our design, binary valves and the PWM method were implemented to take advantage of the compact form factor of the binary valves. All the experiments were done using lab-bench air supply. The source air pressure was 570 kPa with a flow rate of 19 Lpm during the experiments.

The characterization experiment was divided into three phases: dorsiflexion, hold, and plantarflexion. During the dorsiflexion phase, the system fully contracted all three anterior muscles while releasing the posterior muscle to reach the maximum dorsiflexion angle. Then, the system held the dorsiflexion angle by closing all the valves. Finally, the system fully contracted the posterior muscle while releasing the anterior muscles to reach maximum plantarflexion. In this experiment, we were able to achieve different contraction and release speeds of the pneumatic muscles by changing the duty cycle of the PWM controller. The result, shown in figure 8(*a*), shows the maximum achievable range of ankle motion was

Table 1. Pneumatic muscle geometries and gas consumptions when fully contracted (air pressure: 570 kPa).

Muscle	Radius (cm)	Length (cm)	Volume (cm^3)	Air (g)	CO_2 (g)
M1	1	13.5	42.4	0.31	0.47
M2	1	12	47.7	0.28	0.42
M3	1	10.5	33.0	0.24	0.37
M4	1	15	47.1	0.34	0.51
Total				1.17	1.77

$27°$ ($14°$ dorsiflexion and $13°$ plantarflexion) for the case study subject.

We also tested repeated dorsiflexion and plantarflexion. The system carried out the characterization program continuously for about 2 min. The result, figure 8(*b*), shows the system could achieve the same angles reliably. While the target angles were obtained, the angle held gradually decreased during the holding phase due to air leakage of the valves. Thus, feedback control is necessary for more accurate joint angle control, which will be discussed in section 4.

3.3. Power consumption

3.3.1. Electric power. The system consumes relatively small electric power as the actuation is pneumatically powered. Three rechargeable lithium-ion batteries (3.7V-900mAh, Sparkfun Electronics, Boulder, CO 80301, USA) provide enough power to operate the entire system for more than 2 h. The control hardware, excluding the solenoid valves, requires 2.5 W, and the valve circuits require 1.5 W on average.

3.3.2. Pneumatic gas consumption. Pneumatic power consumption can be analyzed based on the pressure and the volume of the compressed air consumed for actuation using the ideal gas law. The volume of air can be calculated from the geometry of the contracted muscles. Assuming the gas is consumed isothermally, and the molar masses of air and CO_2 are 29 g and 44 g, respectively, the four muscles consume the total of either 1.17 g of air or 1.77 g of CO_2 in one full actuation. Table 1 summarizes the geometry and gas consumption of each muscle when contracted with pressure of 570 kPa. For portability, a commercially available cylinder (5GAR9, W. W. Grainger Inc., Lake Forest, IL 60045, USA) that contains 567 g of liquid CO_2 at 827 kPa can be carried with the device. One cylinder can provide more than 320 full actuation cycles of all four muscles assuming isothermal gas consumption.

4. Control

Once the basic characterization of the sensing and actuation systems interacting with the human subject is completed, a model-based feedback controller is designed such that the orthotic system is used to track desired ankle angular trajectories. The development of such a controller poses several challenges, which need to be resolved in order to meet the desired requirements of the orthotic system as a rehabilitation tool. Numerous complexities arise as the combined human-orthotic system is a complex plant where relevant parameters, such as the ankle stiffness of a given individual or the actuator speed, are unknown or difficult to estimate. These complexities make modeling from first principles very difficult. Also, in general, it is not uncommon that highly complex systems exhibit nonlinear dynamics that are not easy to model with *a priori* information only. Further difficulties arise from the injection of unexpected voluntary or involuntary disturbances by the human subject, which demand a control system capable of rejecting low- and medium-frequency disturbances. A third set of challenges reflects the fact that, in general, pneumatic actuators are not easy to model and control. In particular, although the actuators of the kind considered here are lightweight, compliant, and capable of generating large forces, it has been argued that pneumatic actuators have not been widely used in rehabilitation and assistive robotics because they are difficult to control [38]. McKibben pneumatic artificial muscles, for example, are very challenging to model from first principles or characterize dynamically, and thus, they have been primarily modeled using a static approach [39, 40]. This might explain that, to date, the pneumatic robotic systems in which sophisticated control strategies have been implemented are composed of rigid moving parts [38, 41, 42], and that, when artificial muscles have been used, the control strategies are mostly model-free, tuning-based or based on heuristic methods such as fuzzy logic [43–45].

There exists an extensive literature on first-principles-based static modeling of McKibben artificial muscles, in which the objective has been to find relationships between the actuator tension, length, and air pressure [39, 40, 46]. This line of research is useful for understanding the capabilities and limitations of the actuators. However, static modeling is not sufficient for devising trajectory-following high-performance controllers. An alternative approach follows from observing that, under controlled experimental conditions, the McKibben actuator exhibits a behavior that can be modeled as a second-order system that maps the effective force generated by the contractile element to the resulting actuator displacement, provided that the actuation pressure remains constant [43, 47]. This kind of model depends on three parameters that can be interpreted as a mass, a spring coefficient and a damping coefficient, which depend on the actuation pressure. Thus, assuming small variations of the actuation pressure and using appropriate sensors, a control strategy to follow a desired actuation displacement. However, for angular trajectory following, this is not practical because we still need a way to exactly specify and generate the required effective force. Furthermore, estimating only two parameters for a fixed-structure low-order model almost certainly would not capture the complex dynamics of the system proposed here.

Considering the issues described above, we avoid modeling the robotic-human system from first principles and instead treat the system as a black box for which we estimate an input–output LTI dynamic mapping, using a subspace system identification technique. Once a model of the system is found through system identification, a model-based single-input–single-output (SISO) LTI controller is designed. The idea of treating this complex robotic configuration, which mechanically interacts with a human leg, as a black box is

experimentally validated by evaluating the performance of the proposed control strategy for several predetermined angular references. It is important to mention that classical and modern synthesis techniques have been recently used in the design and implementation of controllers for active hard robotic prosthetic systems [38, 41, 42, 48–50]. In the work presented in this paper, we expand the use of model-based control strategies to the soft architecture described in the previous sections of this paper. The specific solution proposed in this research is described in the following subsections. Here, $\mathbb{R}$, $\mathbb{R}^{++}$, and $\mathbb{Z}^+$ denote the sets of real, strictly positive real, and non-negative integer numbers, respectively. The variable t is used to index discrete time, i.e., $t = \{kT_s\}_{k=0}^{\infty}$, with $k \in \mathbb{Z}^+$ and $T_s \in \mathbb{R}$, where T_s is the sampling-and-hold time. The variable τ denotes continuous-time. z^{-1} denotes the delay operator, i.e., for a signal x, $z^{-1}x(k) = x(k-1)$ and conversely $zx(k) = x(k+1)$. In this case, z is also the complex variable associated to the z-transform.

4.1. Inputs, outputs, and system identification

From an upper-level input–output perspective we can identify three major subsystems of interest that compose the robotic system: the solenoid valves (and the associated electronic low-level controller), the four pneumatic muscles, and the strain sensor, used to measure the ankle joint angle. Here, we focus on sagittal plane control (dorsiflexion and plantarflexion), which implies that the set of physical valves can be represented as a subsystem composed of two abstract valves (an injection valve and a release valve), each of which is in one possible state: *open* or *closed*. Thus, the set containing the three anterior muscle injection valves and the posterior muscle release valve is modeled as one abstract injection valve. Similarly, the set containing the three anterior muscle release valves and the posterior muscle injection valve is modeled as one abstract release valve. The ankle joint angle is the controlled variable, which is measured with the custom-built strain sensor, previously described.

Since there are eight physical valves and the subject foot is allowed to rotate in space, the original problem is multiple-input–multiple-output (MIMO). However, the complexity of the problem is greatly reduced by simplifying the movement of the foot to the sagittal degree of freedom and by defining the control signal in an intelligent manner, so that the open-loop mapping becomes SISO. For sagittal plane motions, the four actuators work synchronously, where the three anterior muscles always expand or contract simultaneously, while the posterior muscle performs synchronously the opposite action. Thus, four of the eight solenoid valves are thought of as the abstract element valve 1, and the other four solenoid valves correspond to the abstract element valve 2. We label the states of valve 1 and valve 2, v_1 and v_2, respectively. When a valve is closed, its value is 0, and when open, its value is 1. Thus, the state-space of the entire system is given by

$$v = \begin{bmatrix} v_1 \\ v_2 \end{bmatrix} \in \left\{ \begin{bmatrix} 0 \\ 0 \end{bmatrix}, \begin{bmatrix} 0 \\ 1 \end{bmatrix}, \begin{bmatrix} 1 \\ 0 \end{bmatrix} \right\}, \tag{5}$$

where the vector $[1 \quad 1]^T$ is not an allowable state. Since there are no dynamic relationships between the *digital signal*
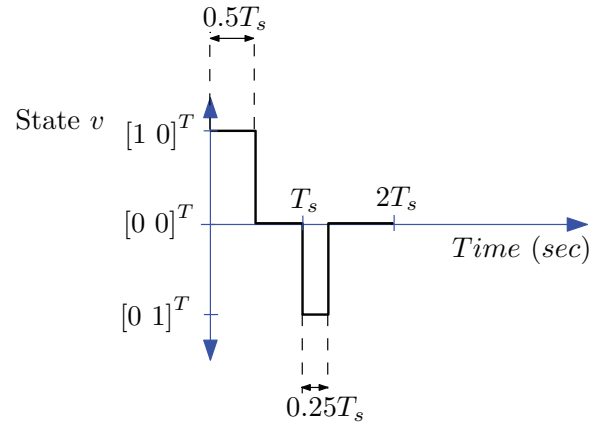
Figure 9. Example of an input signal $u(t)$ written in terms of the state v. In this case $u(0) = 0.5$ and $u(1) = -0.25$.

processor (DSP) output and the state v, the input $u(t)$ can be defined directly in terms of the state v. We can think of this as a one-to-one mapping between $u(t)$ and the history of v over the valve-cycle starting at time t. In order to describe this mapping, we say that a valve-cycle starts when v changes from $[0 \quad 0]^T$ to one of the other two allowable states in (5), i.e., a valve-cycle starts when one and only one of the two valves is opened. Some time after one of the valves is opened, this is closed and remains in this position until a new cycle starts. Here, the duration of each valve-cycle is fixed at T_v, which is chosen to coincide with the sample-and-hold time used for signal processing and control, T_s. Therefore, we completely define the valve-cycle starting at the discrete time t as follows below.

Definition 1. *In terms of the input signal $u(t) \in [-1, 1]$, the valve-cycle at time t is defined according to the rules.*

- *If $u(t) \geqslant 0$, the corresponding valve-cycle starts with $v = [1 \quad 0]^T$ and stays this way for an amount of time equal to $|u(t)|T_s$, then the state switches to $v = [0 \quad 0]^T$ and stays this way for the rest of the valve-cycle.*
- *If $u(t) < 0$, the corresponding value-cycle starts with $v = [0 \quad 1]^T$ and stays this way for an amount of time equal to $|u(t)|T_s$, then the state switches to $v = [0 \quad 0]^T$ and stays this way for the rest of the valve-cycle.*

Definition 1 allows one to formulate a SISO LTI identification problem, and consequently, to use classical model-based controller design techniques. Here, we illustrate definition 1 through a simple example. Figure 9 shows an input signal $u = \{u(0), u(1)\}$, with $u(0) = 0.5$ and $u(1) = -0.25$. Since $u(0) > 0$, the valve-cycle corresponding to $Time = 0$ s starts with $v = [1 \quad 0]^T$, and since $|u(0)| = 0.5$, it follows that $v = [1 \quad 0]^T$ for $0.5T_s$ s, and then, $v = [0 \quad 0]^T$ for the rest of the valve-cycle. Similarly, since $u(1) < 0$, the valve-cycle corresponding to $Time = 1$ s starts with $v = [0 \quad 1]^T$, and since $|u(1)| = 0.25$, it follows that $v = [0 \quad 1]^T$ for $0.25T_s$ s, and then, $v = [0 \quad 0]^T$ for the rest of the valve-cycle.

In this way, the signal $u(t)$ simultaneously conveys two pieces of information at each discrete time t. The
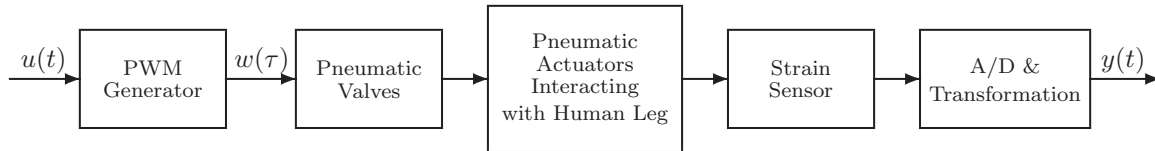
Figure 10. Upper-level physical description of the system from an input–output perspective, according the definitions of $u(t)$ and $y(t)$. Note that $y(t)$ is a physical variable (angular position), whereas $u(t)$ is not a physical entity but a mathematical tool used for controller design.
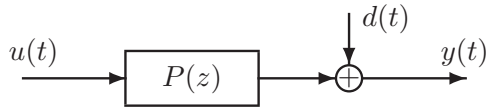
Figure 11. Idealized system dynamics. $P(z)$: discrete-time open-loop plant; $u(t)$: input signal; $y(t)$: measured sagittal ankle angle; $d(t)$: output disturbance, representing the aggregated effects of all the disturbances affecting the system.

sign of $u(t)$ provides the state, v, with which the valve-cycle starts at time t, and the magnitude of $u(t)$ determines how long the state v remains different from $[0 \quad 0]^T$ during the corresponding valve-cycle. The whole process can be regarded as a mapping that transforms the discrete-time signal $u(t)$ to a two-dimensional analogous PWM signal, $w(\tau) = [w_1(\tau) \quad w_2(\tau)]^T$, where w_1 activates valve 1 and w_2 activates valve 2. Naturally, the choice for the system output is the sagittal ankle joint angle measured by the strain sensor, labeled as $y(t)$.

The definition of $u(t)$ and the upper-level idealization in figure 10 allows one to think of the system as a black box that maps the digital input $u(t)$ to the digital output $y(t)$, where the sampling-and-hold time for signal processing and control is $T_s = T_v$. Thus, assuming an LTI system, P, an equivalent block-diagram is depicted in figure 11, where $d(t)$ is an output disturbance representing the aggregated effects of all the disturbances affecting the system. The system described by this block-diagram can be estimated using well-known subspace system identification methods that yield state-space realizations of LTI systems, i.e., $\{A_P, B_P, C_P, D_P\}$ matrices describing the system according to

$$x_P(t+1) = A_P x_P(t) + B_P u(t), \qquad (6)$$

$$y(t) = C_P x_P(t) + D_P u(t) + d(t), \qquad (7)$$

where, $x_P(t) \in \mathbb{R}^n$ is the n-dimensional vector state of the state-space realization $\{A_P, B_P, C_P, D_P\}$, describing P. A realization is called minimal if the system described by (6)–(7) is both observable and controllable. The main advantage of using subspace identification methods is that the order of the system to be identified does not have to be assumed *a priori*, and therefore, the resulting realizations are always minimal.

Using the algorithm in [51], with the implementation described in [52], the system in figure 11 is identified with the use of 50 000 samples generated using a uniform white-noise signal input $u(t) \in [-1, 1]$, at a sample-and-hold rate of 50 Hz, i.e., a sampling time $T_s = 0.02$ s. We use white noise to excite the system over the entire sampled spectrum, 0 Hz to the Nyquist frequency, 25 Hz [53, 54]. In the experiments performed for identifying the system, the same subject sits
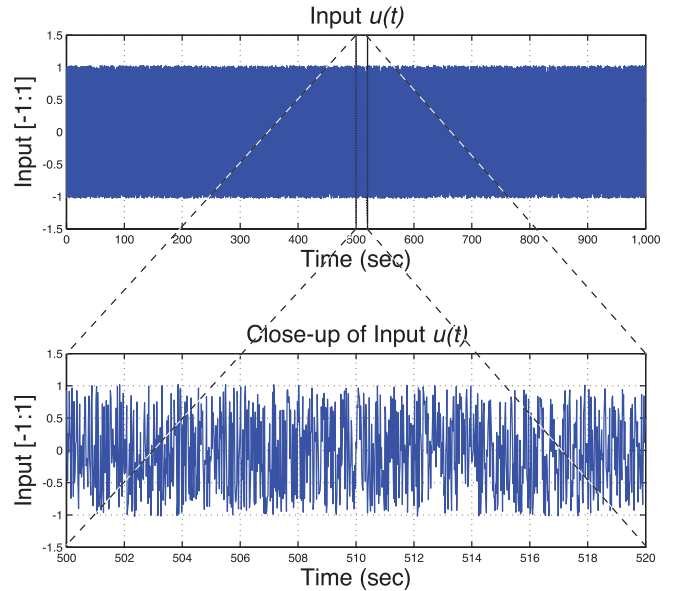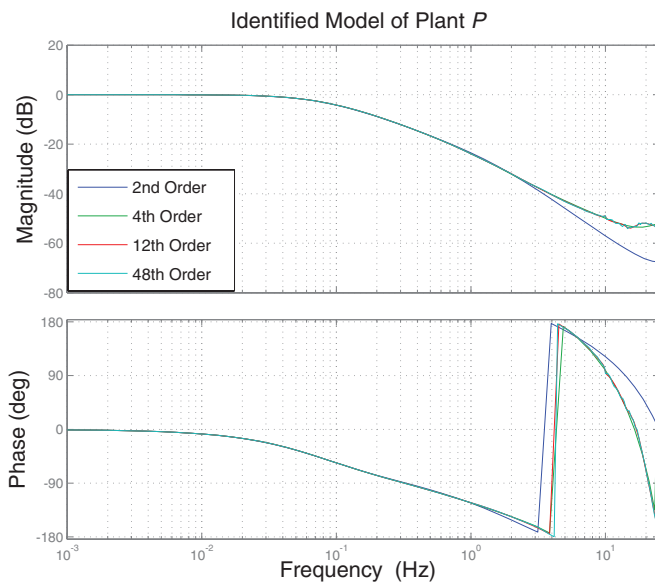

Figure 12. Input signal used in the LTI system identification of the plant *P*. *Upper plot:* complete input sequence used in the system identification. This is white noise, where each data point is the realization of a uniform distribution. The compactness of the plot (the blue rectangular spot) is a reflection of the high frequency content of the signal. *Bottom plot:* close-up of the input signal used in the system identification. This segment shows 20 s of the signal.

on a rigid bench while his leg hangs freely, as described in section 3. Figures 12 and 13 show the input and output signals used in the LTI system identification of the plant *P*.

The resulting identified dynamics of $P(z)$, labeled as $\hat{P}(z)$, are shown in figure 14. The original 48th-order model identified is shown along with reduced order models with orders 12, 4, and 2, respectively. Since the highest frequencies in recorded ankle joint angle signals are smaller than 2 Hz [55], it is clear that the system dynamics can be represented by the low-pass second-order LTI filter in figure 14. The identified systems have been normalized so that the respective dc gain is 0 dB and the cutoff frequency of $\hat{P}$ is approximately 0.1 Hz. A cutoff frequency of approximately 2 Hz has been reported for McKibben type actuators [21], which indicates that in the case considered here, the cutoff frequency of 0.1 Hz reflects the effect of the mechanical impedance of the user's limb, but more importantly, the slow response of the solenoid valves used to generate the PWM signals. In order to reduce the order of the system, a state-space realization of the identified 48th-order model is balanced [56], and then, a certain number of states, relatively less observable and controllable than the others, are discarded, as explained in [56]. Here, the identified models were validated using the standard practice of simultaneously
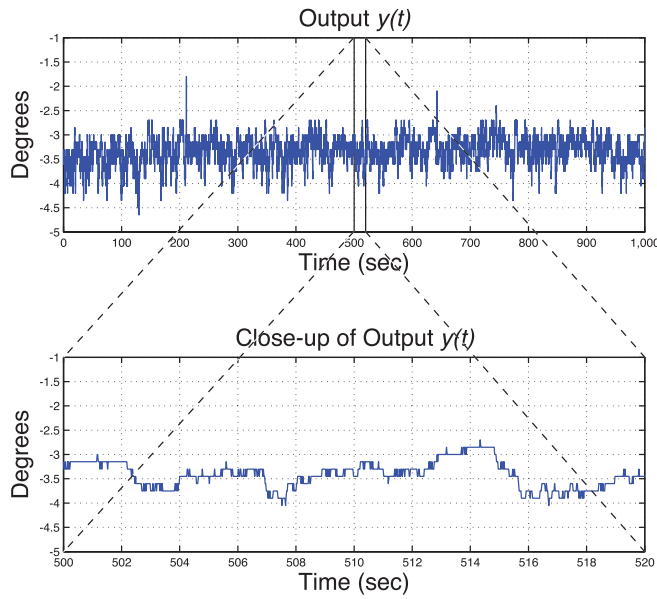
Figure 13. Output signal used in the LTI system identification of the plant *P*. *Upper plot:* complete output sequence used in the system identification. *Bottom plot:* close-up of the output signal used in system identification. This segment shows 20 s of the signal.


Figure 14. Bode plot of the identified model $\hat{P}$ of *P*. A 48th-order model is originally identified, then reduced order models with 12, 4 and 2 states are found, using the balanced reduction method. These systems have been normalized so that the respective dc gain is 0 dB.

exciting the estimated model and the physical system with the same signal and then compare the respective outputs [53, 54].

4.2. Controller implementation and design

4.2.1. Control software implementation. The system identification presented in subsection 4.1 and the controller design described in this subsection are implemented and tested on the main DSP (8-bit Atmel Atmega1280 MCU clocked at 8 MHz with 8 KB RAM). In order to implement and run the closed-loop algorithm, the strain sensor signal is
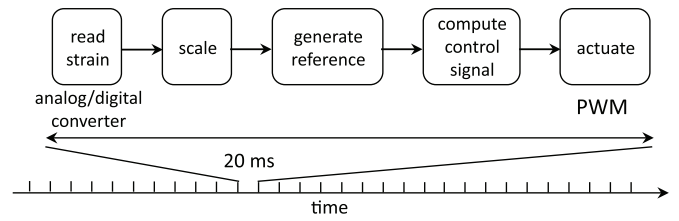
Figure 15. Implementation of the control loop at the machine level, using five basic computing functions. The control loop is scheduled to run every 20 ms. (The total time of each loop is 20 ms.)
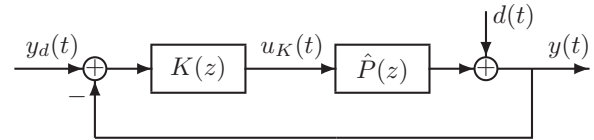
Figure 16. Idealized closed-loop configuration used in the design of the controller $K(z)$. The signal $u_K(t)$ is not directly applied to the system $P(z)$, but used in the definition of the control strategy in (8).

sampled, the control signal $u(t)$ computed, and then using the information in $u(t)$, PWM commands are sent to the solenoid valves that activate the actuators. The algorithms processing the signals required for the control loops are run at 50 Hz, limited by the response time of the solenoid valves (20 ms).

When the sensor signal is converted to an angle, a reference input is either generated from a predefined trace or computed in real time from an input function. Both the measured joint angle and the reference are then fed into a higher level control algorithm, to be discussed in the next part of this subsection, which produces actuation parameters according to definition 1 for the solenoid valves. The PWM duty cycles of the valves are then set according to the control algorithm output in order to contract or release the pneumatic artificial muscles. Figure 15 illustrates the implementation of the control loop at the machine level, using five computing functions.

4.2.2. Upper level controller design. At an upper-level, using definition 1, controller design means that we are interested in finding rules for generating the input signal $u(t)$ so that the output signal $y(t)$ follows a reference $y_d(t)$ and the control error $e_y(t) = y_d(t) - y(t)$ is minimized according to some metric. With this in mind, we propose a nonlinear control law with the form

$$u(t) = \begin{cases} 1 & \text{if } u_K(t) \geqslant 1 \\ u_K(t) & \text{if } -1 < u_K(t) < 1 \\ -1 & \text{if } u_K(t) \leqslant -1 \end{cases} \quad (8)$$

with

$$u_K(t) = [K(z)e_y](t), \quad (9)$$

where $K(z)$ is an LTI controller designed using the information contained in $\hat{P}$, as defined in subsection 4.1. A depiction of the idealized perfectly linear model used for controller design is shown in figure 16. Considering that the defined input–output system *P* relies on definition 1 and that $\hat{P}$ was found around a specific operating point, *K* must be designed not only to improve the system performance but also to meet minimum
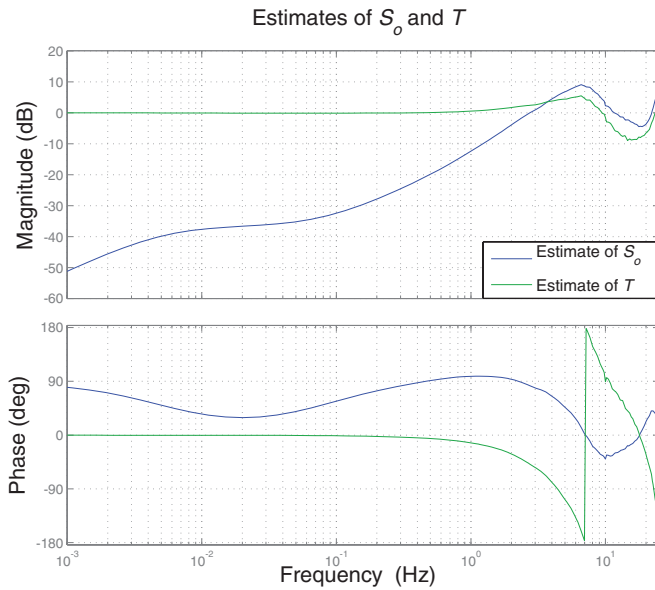
Figure 17. Bode plots of the estimated output sensitivity and complementary sensitivity functions $\hat{S}_o = (1 + \hat{P}K)^{-1}$ and $\hat{T} = \hat{P}K(1 + \hat{P}K)^{-1}$ of S_o and T, respectively. $\hat{S}_o$ is plotted in blue and $\hat{T}$ is plotted in green. The cutoff frequency of the high-pass filter $\hat{S}_o$ is between 4 and 5 Hz, which indicates that the idealized nominal control system in figure 16 is capable of rejecting low-frequency disturbances generated by involuntary movements of the human subject. The shape of $\hat{T}(z)$ demonstrates that the controller $K(z)$ significantly increases the bandwidth of the system.

standards of robustness with respect to plant uncertainty. In this case, plant uncertainty is expected as the device interacting with a human leg results in highly complex dynamics. The controller K must also be designed such that, in closed loop, the system rejects low-frequency disturbances, desired trajectories can be followed, and the gain and phase margins are large enough to ensure stability and performance robustness to plant uncertainties.

The first two capabilities required from the resulting closed-loop system are examined using the output disturbance sensitivity and complementary sensitivity functions

$$S_o = \frac{1}{1 + PK}, \quad T = \frac{PK}{1 + PK}, \quad (10)$$

which can be estimated as $\hat{S}_o = (1 + \hat{P}K)^{-1}$ and $\hat{T} = \hat{P}K(1 + \hat{P}K)^{-1}$, respectively. Bode plots of both estimated plants, for the system parameters defined in subsection 4.1, are shown in figure 17. The gain and phase margins are computed from an estimate $\hat{L} = \hat{P}K$ of the loop-gain $L = PK$. The corresponding values are 5.8 dB and 45.9°, approximately, which indicates that the resulting closed-loop system is robustly stable. Note that the control signal $u(t)$ is not a physical entity, but a mathematical tool useful for controller design.

4.3. Experimental results

The suitability of the proposed approach is demonstrated through six different sets of experiments. The first set is shown in figure 18 and table 2. In this experiment, the system is required to follow sinusoidal references with a fixed
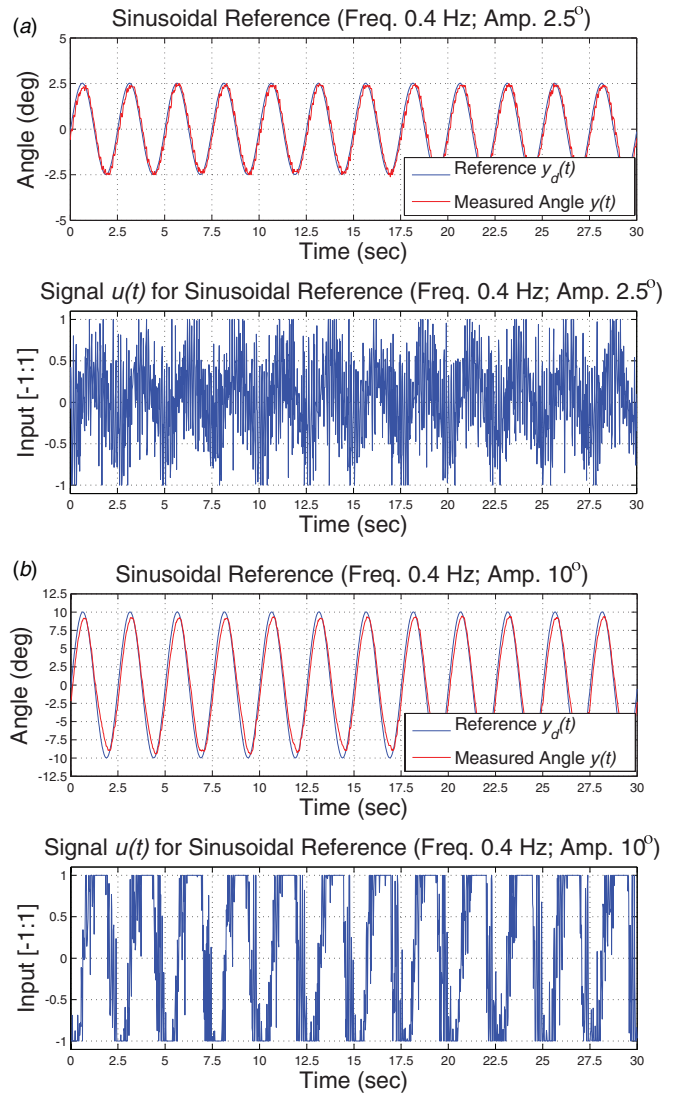
Figure 18. *First set of experiments.* In both experimental cases, (*a*) and (*b*), the *upper plot* shows the time-series of the reference signal $y_d(t)$ and the measured angular position $y(t)$, the controlled variable. In both cases, the *bottom plot* shows the time-series of the corresponding signal $u(t)$. In case (*a*), the reference is a sinusoid with amplitude 2.5° and frequency 0.4 Hz. In case (*b*), the reference is a sinusoid with amplitude 10° and frequency 0.4 Hz.

frequency of 0.4 Hz, with amplitudes of 2.5°, 5°, 7.5° and 10°, while the subject is sitting on a bench with his foot hanging. The experiments corresponding to amplitudes of 2.5° and 10° are shown in figure 18. The performance of each of the amplitudes considered here (2.5°, 5°, 7.5° and 10°) is shown in table 2. The performance is measured using the *experimental standard deviation* (ESD) of the control error signal, expressed as a percentage of the reference angle range. In both cases in figure 18, the upper plot shows the time-series of the chosen reference and the resulting measurement, and in each case, the bottom plot shows the corresponding control signal $u(t)$. Note that the results in case 1(*a*) are in close agreement with what is predicted by the estimated complementary function $\hat{T}$ in figure 17, in terms of performance. This consistency is explained by the fact that for a sinusoidal reference with an amplitude of

Table 2. Performance measured as the *experimental standard deviation* (ESD) of the control error, expressed as a percentage of the angle range $\left(100\% \frac{\text{STD}(\textit{Control error})}{\textit{angle range}}\right)$.

|	Signal amplitude					
Experimental case	2.5°	5°	7.5°	10°	Low (figure 23(a))	High (figure 23(b))
Case 1 (0.4 Hz sine)	7.2%	7.3%	7.1%	7.4%	N/A	N/A
Case 2 (0.4 Hz sine + disturb.)	11.5%	10.6%	10.4%	8.6%	N/A	N/A
Case 3 (0.8 Hz sine)	11.7%	10.7%	14.2%	16.0%	N/A	N/A
Case 4 (1.0 Hz sine)	14.5%	17.2%	17.7%	20.2%	N/A	N/A
Case 5 (Walking gait)	N/A	N/A	N/A	N/A	12.9%	17.2%
Case 6 (Square wave)	18.5%	20.9%	24.2%	26.4%	N/A	N/A

2.5°, the behavior of the system can be considered LTI, as $u_K(t)$ rarely saturates and $u(t) \approx u_K(t)$, as evidenced from the bottom plot in figure 18(*a*). In the case shown in figure 18(*b*), it is clear that the measured signal $y(t)$ closely follows the reference $y_d(t)$. However, as shown in table 2, as the amplitude of the reference increases, a progressive deterioration in performance can be observed, caused by the saturation of the signal $u_K(t)$, according to the law in (8). The saturation of $u_K(t)$ reflects the physical inability of the robotic orthotic system to contract and expand at the speeds required by the linear control law defined by $K(z)$. The notion that the saturation of $u_K(t)$ is caused by a speed constraint follows from simply noticing that, for a fixed frequency, the required contraction and expansion speeds of the artificial muscles are directly proportional to the amplitude of the reference $y_d(t)$, i.e.,

$$s_d(t) = A_g A_d \omega \cos(\omega t), \tag{11}$$

where $s_d(t)$ is the desired speed of contraction and expansion, ω is a fixed frequency, $A_g \in \mathbb{R}^{++}$ is a geometric constant, and A_d is the amplitude of the angular reference. Note that the speed of a McKibben actuator depends on the actuator itself, but also on the actuation pneumatic valves, which in this case are the main cause of speed limitation.

The last plots associated with case 1 are shown figure 19, which is an example of the mapping from u to v. An interesting thing to notice in figure 19 is that, as described in definition 1, if the signal u does not hit the saturation limits, the idealized valve's state v changes during a time cycle. In other words, in the system considered here, saturation means that the idealized valve's state v stays constant over the whole time cycle.
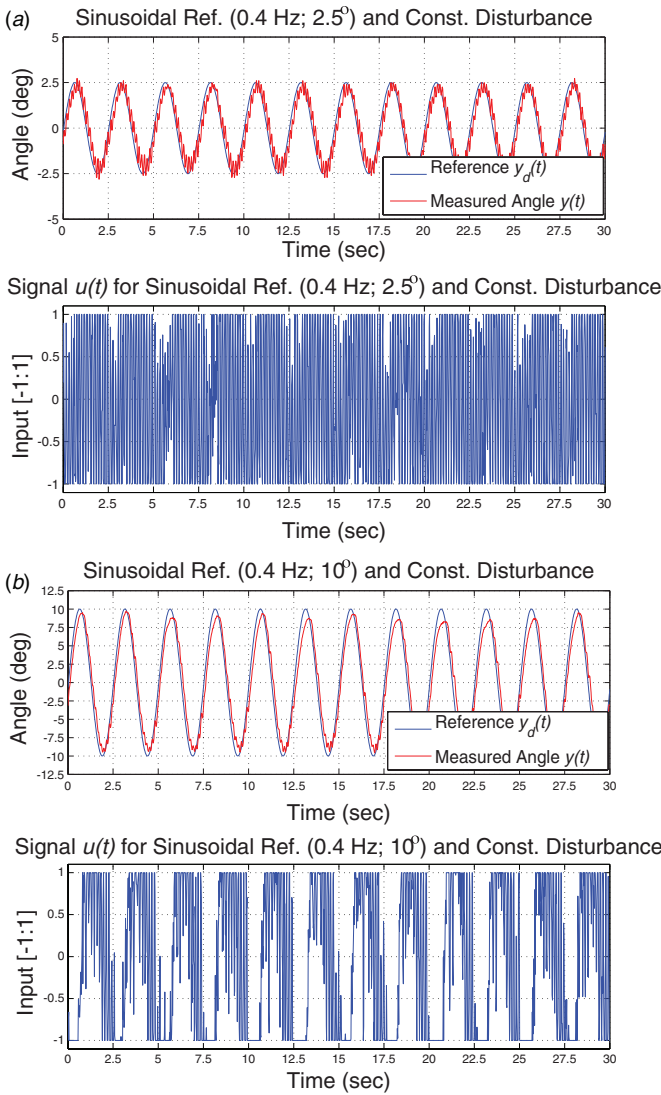
In the second set of experiments, the objective is to test the system when subjected to a significant constant force disturbance. In this case, a large weight (500 g) counteracting the dorsiflexion of the subject's leg is hanged at the distal end of the foot, which experimentally simulates the case of patients with highly contracted gastrocnemius muscles, a typical characteristic of a drop foot symptom in CP. The chosen references are the same used in the first set of experiments. In both cases shown in figure 20, it is clear that the measured signal $y(t)$ closely follows the reference $y_d(t)$, and overall, the achieved performance is good enough to suggest that the robotic orthotic system could be employed as a rehabilitation device. Note that in this case, as shown in table 2, for each amplitude considered (2.5°, 5°, 7.5°, 10°), the resulting performance is degraded with respect to case 1, due to the
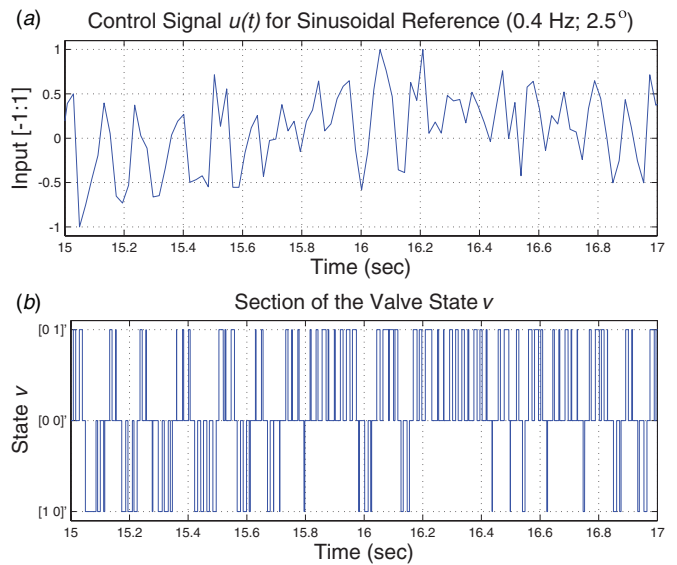
Figure 19. *Upper plot:* short section of the time-series of $u(t)$ from the experimental case 1(*a*). *Bottom plot:* resulting valve's state $v(\tau)$, corresponding to the section of $u(t)$ in the upper plot.
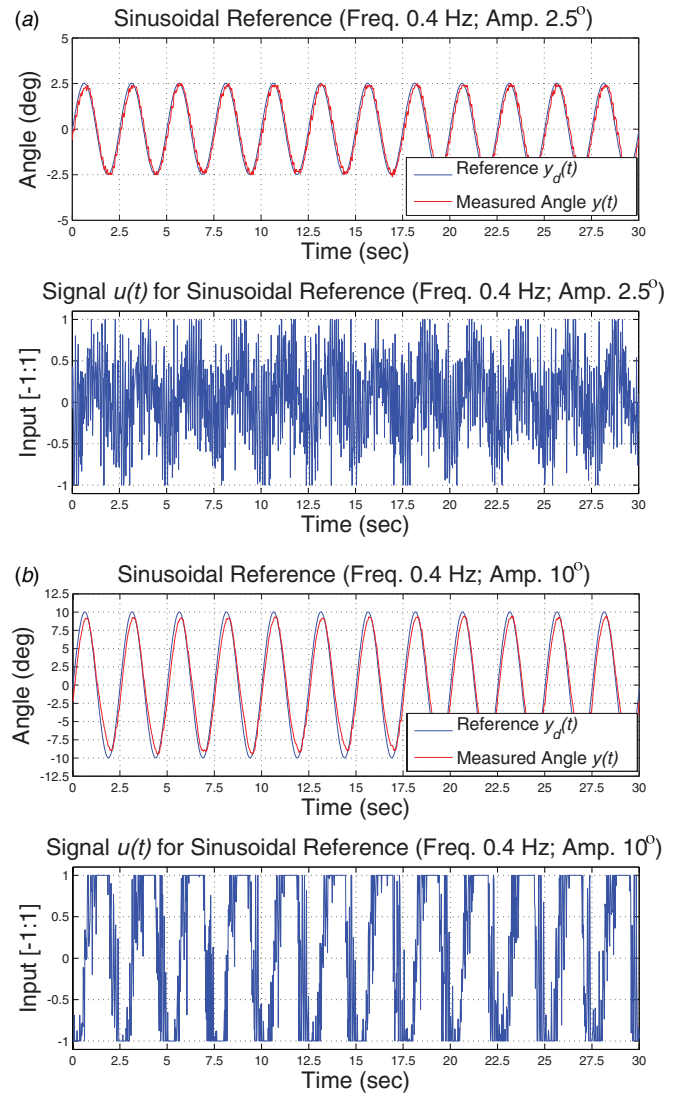
effect of the force disturbance acting on the system. Recall that here, performance is measured using the ESD of the control error signal as a percentage of the reference angle range. Interestingly, in case 2, as can be observed in figure 20, as the percentage performance in table 2 improves with amplitude, the absolute control error increases with amplitude. The first phenomenon is explained by the saturation of $u_K(t)$ caused by the speed constraint of the actuators, already discussed above. The second phenomenon can be explained by noticing that the most notable effect produced by the force disturbance is a high frequency oscillation over the measured signal $y_d(t)$, which has an amplitude that stays approximately constant as the reference angle's amplitude is varied. The existence of this high frequency content is the direct result of the orthotic system's slow response speed. Overall, the capability of the closed-loop system to reject disturbances, according to what is predicted by the estimate of $\hat{S}_o$ in figure 17, is demonstrated in figure 20(*a*). This indicates that the chosen control strategy is adequate for this kind of system and that the limitations in performance reflect physical limitations of the hardware. The performances of all the variants of case 2 are shown in table 2.

Figures 21 and 22 show the experimental sets 3 and 4, which are aimed at testing how well the system performs at

Figure 20. *Second set of experiments.* In both experimental cases, (*a*) and (*b*), the system is subjected to the force constant disturbance. In both cases, (*a*) and (*b*), *upper plot* shows the time-series of the reference signal $y_d(t)$ and the measured angular position $y(t)$, the controlled variable. In both cases, the *bottom plot* shows the time-series of the corresponding signal $u(t)$. In case (*a*), the reference is a sinusoid with amplitude 2.5° and frequency 0.4 Hz. In case (*b*), the reference is a sinusoid with amplitude 10° and frequency 0.4 Hz.

Figure 21. *Third set of experiments.* In both experimental cases, (*a*) and (*b*), *upper plot* shows the time-series of the reference signal $y_d(t)$ and the measured angular position $y(t)$, the controlled variable. In both cases, the *bottom plot* shows the time-series of the corresponding signal $u(t)$. In (*a*), the reference is a sinusoid with amplitude 2.5° and frequency 0.8 Hz. In (*b*), the reference is a sinusoid with amplitude 10° and frequency 0.8 Hz.

higher required speeds, demonstrate the controller capabilities and expose situations where the limitations of the hardware design come into play. In case 3(*a*) and (*b*), the references are sinusoids with a fixed frequency of 0.8 Hz, with amplitudes 2.5° and 10°, respectively. In case 4(*a*) and (*b*), the references are sinusoids with a fixed frequency of 1.0 Hz, with amplitudes 2.5° and 10°, respectively. The results in figures 21(*a*) and 22(*a*) show that the proposed control strategy is adequate, as predicted by $\hat{S}_o$ and $\hat{T}$. However, figures 21(*b*) and 22(*b*) unequivocally demonstrate that the system is subjected to a hard physical speed constraint. This follows from noticing that the desired speed of contraction and expansion $s_d(t)$ is directly proportional to the reference frequency ω, as shown

in (11). The resulting performances of all the variants of cases 3 and 4 are also shown in table 2.
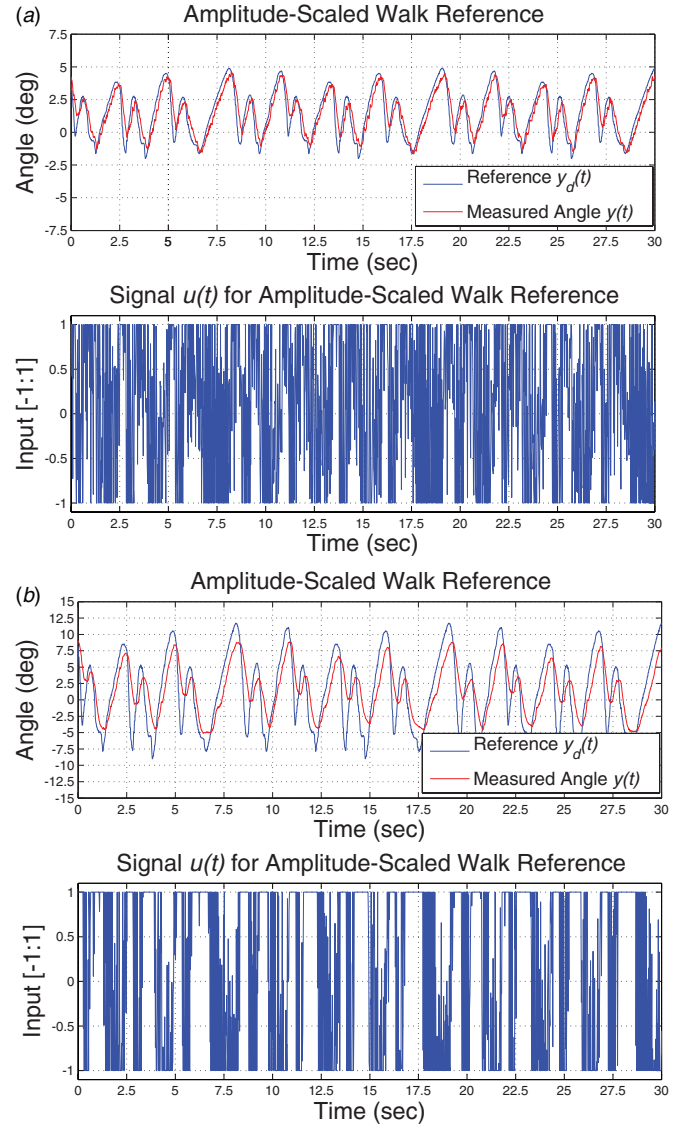
Figure 23 shows the experimental set 5. In case 5(*a*), the reference is an experimentally-recorded amplitude-scaled walk signal. As expected from the experimental cases already shown and from figure 17, it is clear that the measured signal $y(t)$ closely tracks the reference $y_d(t)$. However, despite the fact that the amplitude of the desired output $y_d(t)$ has a relatively small amplitude, the signal $u_K(t)$ saturates repeatedly. This phenomenon is due to the higher frequency content, in comparison to the signals considered in the previously presented cases, in this new reference. References with higher frequency content imply higher requirements of contraction and expansion speeds from the artificial muscles. As expected, the saturation phenomenon becomes worse when the walking reference signal is scaled to a magnitude similar
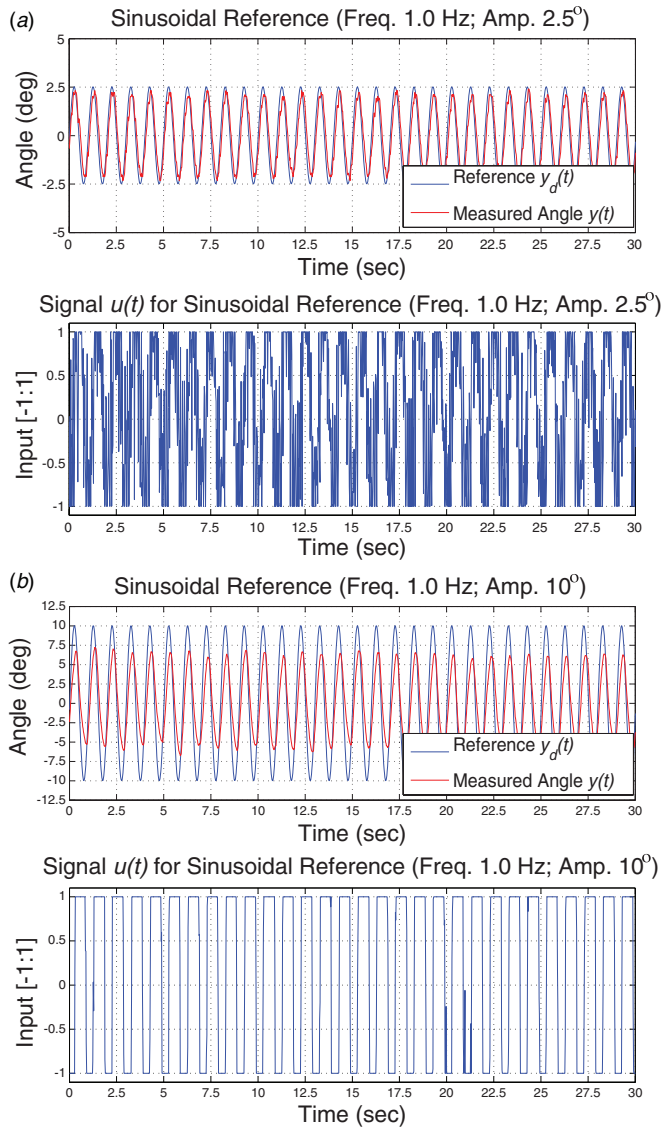
Figure 22. *Fourth set of experiments.* In both experimental cases, (*a*) and (*b*), *upper plot* shows the time-series of the reference signal $y_d(t)$ and the measured angular position $y(t)$, the controlled variable. In both cases, the *bottom plot* shows the time-series of the corresponding signal $u(t)$. In (*a*), the reference is a sinusoid with amplitude 2.5° and frequency 1.0 Hz. In (*b*), the reference is a sinusoid with amplitude 10° and frequency 1.0 Hz.

Figure 23. *Fifth set of experiments.* In both experimental cases, (*a*) and (*b*), *upper plot* shows the time-series of the reference signal $y_d(t)$ and the measured angular position $y(t)$, the controlled variable. In both cases, the *bottom plot* shows the time-series of the corresponding signal $u(t)$. In case (*a*), the reference is an amplitude-scaled walking signal ranging from $-1°$ to 5°, approximately. In case (*b*), the reference is an amplitude-scaled walking signal ranging from $-10°$ to 12.5°, approximately.

to those in the technical literature showing normal walking patterns [55], as shown in figure 23(*b*). Despite the saturation issue, the experiments in figure 23 present compelling evidence on the robotic orthotic system capabilities to be employed in rehabilitation and on the potential capabilities as a walking assistive device. The resulting performances of case 4 are shown in table 2.

Figure 24 shows the experimental set 6. In case 6(*a*), the reference is a 0.1 Hz-square-wave with an amplitude of 2.5°. In case 6(*b*), the reference is a 0.1 Hz-square-wave with an amplitude of 10°. These cases clearly show the capabilities and limitations of the robotic system. From both cases it follows that the maximum angular speed achievable by the system is $14° \, \mathrm{s}^{-1}$, approximately. Also, as predicted by figure 17, it follows that the control strategy is adequate for

tracking constant signals, which adds evidence to the notion that the proposed robotic system has a substantial potential as a rehabilitation device. Finally, notice that the saturation phenomenon appears in both cases, more dramatically underlined in figure 24(*b*). The resulting performances of all the variants of case 6 are shown in table 2.

5. Discussion and future work

The main contribution of this work is the biologically inspired design and development of a soft wearable robot. The following features make the proposed system novel compared to prior wearable assistive devices.
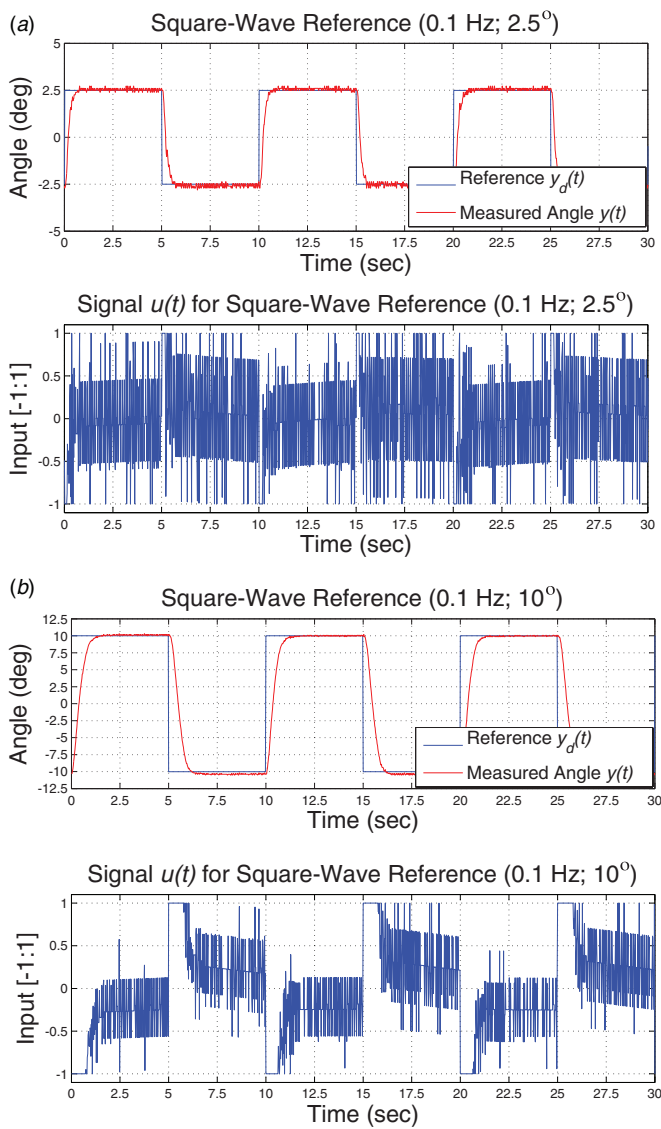
(a)

(b)

Figure 24. *Sixth set of experiments.* In both experimental cases, (*a*) and (*b*), *upper plot* shows the time-series of the reference signal $y_d(t)$ and the measured angular position $y(t)$, the controlled variable. In both cases, the *bottom plot* shows the time-series of the corresponding signal $u(t)$. In case (*a*), the reference is a 0.1 Hz-square-wave with an amplitude of 2.5°. In case (*b*), the reference is a 0.1 Hz-square-wave with an amplitude of 10°.

(i) Bio-inspired actuation system. While most of previous ankle–foot orthotics regard an ankle joint as a simple mechanical pin joint, the proposed device mimics a biological muscle—tendon–ligament architecture with multiple muscles to create various natural ankle motions.

(ii) Soft strain sensors. Hyperelastic strain sensors were developed and implemented to measure joint angles. This type of soft sensors makes the device easily wearable and conformable to complicated 3D body shapes.

(iii) Completely soft structure. The proposed system does not contain any rigid frame structures that are easily seen in other active orthoses, resulting in no constraints on the natural degrees of freedom of the ankle joint.

The current design showed that such an orthotic device has the potential to provide active assistance for ankle

rehabilitation without limiting 3D motion of the foot. The performance of the device when applying a feedback controller was also demonstrated. The current prototype demonstrated full integration of sensing, actuation, and power to create a nearly untethered system.

While the system consumes very little electric power and could run on batteries for several hours, the device still relies on an air source connection for the pneumatic muscles. Thus, one area of on-going work is the investigation of solutions that allow complete untethered operation. Available options include portable air compressors and compressed air canisters. For the long-term success of such orthotic devices, we are also investigating relevant clinical requirements and potential control strategies that would work seamlessly with the user's motion. The goal is to achieve a fully untethered wearable system to provide a new level of mobility and active assistance. This will open a rich space for future rehabilitation techniques both inside and outside of the clinic.

While the system goals for rehabilitation—seated ankle motions—were achieved, the design components could be adapted for increased performance. From an actuation perspective, for example, we could use higher bandwidth actuators and valves. From a control perspective, in order to track angular positions that result from fast walking and running, more sophisticated algorithms are required. In particular, it is possible to represent trajectories similar to the one in figure 23 by linearly combining families of sinusoidal functions. Then, algorithms specialized in tracking families of sinusoidal signals, like multiple-period repetitive control [57], can be used to synthesize feedback controllers. Also, it is possible to use adaptive schemes like the one in [58].

We presented a methodology for synthesizing controllers for a biologically inspired pneumatically-actuated soft orthotic device. The proposed approach relied on system identification and classical LTI design tools. This is surprising and useful, considering that the system to be controlled was highly complex, in which electronic, mechanical, and pneumatic components interact with a human body. Based on experimental data, we presented evidence that by proper choice of the inputs and outputs, classical and modern system-theoretic tools can be implemented for designing high-performance controllers for complex systems.

In this paper, the prototype was tested for seated motions, which have importance for rehabilitation, as a first proof of principle. From this initial testing, we can develop a controller that can assist walking gaits. However, gait assistance is beyond the scope of our current work. Also, while force control may be more appropriate for assisting and supporting dynamic walking—our ultimate goal—the position control result demonstrates the feasibility of our current prototype for use in ankle rehabilitation activities that often consist of various types of seated motions, such as those shown in [59, 60]. These types of seated motions can be easily recorded and replayed using our current device. Nevertheless, force control with dynamic walking should be investigated as the device is upgraded with embedded force sensors in the future.

The subject fully relaxed the ankle while neither intentionally assisting nor resisting the controller's actuation

during the control experiments. Although slight unintentional muscle (or body) reaction to the actuation was reported by the subject during the experiments, it was not strong enough to disrupt the controller. However, this muscle reaction must be taken into account as an internal disturbance for further improvement of the control algorithm. An electromyography is a potential tool to measure the activation of the wearer's biological muscles, which could be treated as disturbance in the control loop.

Although the first set of experimental data presented in this paper focuses only on sagittal motions and SISO control, the current device provides future opportunities for more complex control strategies. For example, a cooperative controller could be designed to achieve more natural ankle motions when controlling individual muscles. Another possible strategy is to implement a supervised learning algorithm to allow the device to assist the user more dynamically without overpowering the natural muscles. This would require the system to learn the user's motion patterns and calculate correct timings to provide timely actuation in order to seamlessly assist the user's intended motions.

Finally, future work will cover various areas. For testing, we plan to perform a clinical study with the system using a clinically appropriate population. For design improvement, we are currently under development of a more generalized form, as shown in [31], to address the issue of individual-dependence. The new design with modularized muscle units that are lightweight and compact will provide the capability of resizing and reconfiguring, which will allow us to easily quantify the manufacturing and characterization cost and the applicability. This new design is also expected to solve several potential problems of the current prototype, such as transmission inefficiency, hardware misalignment, and kinematic constraints. Optimal power control and increased safety is another area that we will investigate for a wide range of users.

6. Conclusions

A bio-inspired soft wearable robotic device was designed and prototyped using soft actuators and sensors. The prototype showed the capability of assisting sagittal ankle motions with actuation, providing a range of $27°$ for our test subject. The prototype also demonstrated the capability for feedback control of ankle joint angle using an identified LTI model of the system. We believe that this bio-inspired design, utilizing soft sensors, actuators, and structures, will open a rich space for future wearable robot and soft robot technologies for human rehabilitation and assistance.

Acknowledgments

References

[1] Winters T F, Gage J R and Hicks R 1987 Gait patterns in spastic hemiplegia in children and young adults *J. Bone Joint Surg.* **69** 437–41

[2] Park Y-L, Chen B, Young D, Stirling L, Wood R J, Goldfield E and Nagpal R 2011 Bio-inspired active soft orthotic device for ankle foot pathologies *Proc. IEEE/RSJ Int. Conf. on Intelligent Robots and Systems (San Francisco, CA)* pp 4488–95

[3] Blanton S, Grissom S P and Riolo L 2002 Use of a static adjustable ankle-foot orthosis following tibial nerve block to reduce plantar-flexion contracture in an individual with brain injury *Phys. Ther.* **82** 1087–97

[4] Mavroidis C *et al* 2011 Patient specific ankle-foot orthoses using rapid prototyping *J. Neuroeng. Rehabil.* **8** 1

[5] Miller F 2005 *Cerebral Palsy* 1st edn (Berlin: Springer)

[6] Yamamoto S, Ebina M, Iwasaki M, Kubo S, Kawai H and Kayashi T 1993 Comparative study of mechanical characteristics of plastic AFOs *J. Prosthet. Orthot.* **5** 59–64

[7] Appell H-J 1990 Muscular atrophy following immobilisation: a review *Sports Med.* **10** 42–58

[8] Geboers J F, van Tuijl J H, Seelen H A and Drost M R 2000 Effect of immobilization on ankle dorsiflextion strength *Scand. J. Rehabil. Med.* **32** 66–71

[9] Geboers J F, Drost M R, Spaans F, Kuipers H and Seelen H A 2002 Immediate and long-term effects of ankle-foot orthosis on muscle activity during walking: a randomized study of patients with unilateral foot drop *Arch. Phys. Med. Rehabil.* **83** 240–5

[10] Bruelmeier M, Dietz V, Leenders K L, Roelcke U, Missimer J and Curt A 1998 How does the human brain deal with a spinal cord injury? *Eur. J. Neurosci.* **10** 3918–22

[11] Green J B, Sora E, Bialy Y, Ricamato A and Thatcher R W 1998 Cortical sensorimotor reorganization after spinal cord injury: an electroencephalographic study *Neurology* **50** 1115–21

[12] Herr H M and Wilkenfeld A 2003 User-adaptive control of a magnetorheological prosthetic knee *Ind. Robot.* **30** 42–55

[13] Lambrecht B G A and Kazerooni H 2009 Design of a semi-active knee prosthesis *Proc. IEEE Int. Conf. on Robotics and Automation (Kobe, Japan)* pp 639–45

[14] Krebs H, Hogan N, Durfee W and Herr H 2005 Rehabilitation robotics, orthotics, and prosthetics *Textbook of Neural Repair and Rehabilitation* ed M E Selzer, S Clarke, L G Cohen, P W Duncan and F H Gage (Cambridge: Cambridge University Press)

[15] Blaya J A and Herr H 2004 Adaptive control of a variable-impedance ankle-foot orthosis to assist drop-foot gait *IEEE Trans. Neural Syst. Rehabil. Eng.* **12** 24–31

[16] Banala S K, Kim S H, Agrawal S K and Scholz J P 2009 Robot assisted gait training with active leg exoskeleton (ALEX) *IEEE Trans. Neural Syst. Rehabil. Eng.* **17** 2–8

[17] Patritti B L, Straudi S, Deming L C, Benedetti M G, Nimec D L and Bonato P 2010 Robotic gait training in an adult with cerebral palsy: a case report *PMR* **2** 71–5

[18] Roy A, Kerbs I, Williams D J, Bever C T, Forrester L W, Macko R M and Hogan N 2009 Robot-aided neurorehabilitation: a novel robot for ankle rehabilitation *IEEE Trans. Robot.* **25** 569–82

[19] Herr H M and Kornbluh R D 2004 New horizons for orthotic and prosthetic technology: artificial muscle for ambulation *Proc. SPIE* **5385** 1–9

[20] Ferris D P, Czerniecki J M and Hannaford B 2005 An ankle-foot orthosis powered by artificial pneumatic muscles *J. Appl. Biomech.* **21** 189–97

[21] Gordon K E, Sawicki G S and Ferris D P 2006 Mechanical performance of artificial pneumatic muscles to power an ankle-foot orthosis *J. Biomech.* **39** 1832–41

[22] Shorter K A, Kogler G F, Loth E, Durfee W K and Hsiao-Wecksler E T 2011 A portable powered ankle-foot orthosis for rehabilitation *J. Rehabil. Res. Dev.* **48** 459–72

[23] Hollander K W, Ilg R, Sugar T G and Herring D 2006 An efficient robotic tendon for gait assistance *J. Biomech. Eng.* **128** 788–92

[24] Svensson W and Holmberg U 2008 Ankle-foot-orthosis control in inclinations and stairs *Proc. IEEE Int. Conf. on Robotics Automation and Mechatronics (Chengdu, China)* pp 301–6

[25] Nikitczuk J, Weinberg B, Canavan P K and Mavroidis C 2010 Active knee rehabilitation orthotic device with variable damping characteristics implemented via an electrorheological fluid *IEEE/ASME Trans. Mechatronics* **15** 952–60

[26] Stirling L, Yu C, Miller J, Wood R J, Goldfield E and Nagpal R 2011 Applicability of shape memory alloy wire for an active, soft orthotic *J. Mater. Eng. Perform.* **20** 658–62

[27] Galiana I, Hammond F L, Howe R D and Popovic M B 2012 Wearable soft robotic device for post-stroke shoulder rehabilitation: Identifying misalignments *Proc. IEEE/RSJ Int. Conf. on Intelligent Robots and Systems (Vilamoura, Portugal)* pp 317–22

[28] Ueda J, Ming D, Krishnamoorthy V, Shinohara M and Ogasawara T 2010 Individual muscle control using an exoskeleton robot for muscle function testing *IEEE Trans. Neural Syst. Rehabil. Eng.* **18** 399–50

[29] Kim S, Spenko M, Trujillo S, Heyneman B, Santos D and Cutkosky M R 2008 Smooth vertical surface climbing with directional adhesion *IEEE Trans. Robot.* **24** 65–74

[30] Park Y-L, Majidi C, Kramer R, Berard P and Wood R J 2010 Hyperelastic pressure sensing with a liquid-embedded elastomer *J. Micromech. Microeng.* **20** 125029

[31] Park Y-L, Chen B, Majidi C, Wood R J, Nagpal R and Goldfield E 2012 Active modular elastomer sleeve for soft wearable assistance robots *Proc. IEEE/RSJ Int. Conf. on Intelligent Robots and Systems (Vilamoura, Portugal)* pp 1595–602

[32] Park Y-L, Chen B and Wood R J 2012 Design and manufacturing of soft artificial skin using embedded microchannels and liquid conductors *IEEE Sensors J.* **12** 2711–8

[33] Slabaugh G 1999 Computing Euler angles from a rotation matrix *Technical Report* City University London www.soi.city.ac.uk/∼sbbh653/publications/euler.pdf

[34] Mengüç Y, Park Y-L, Martinez-Villalpando E, Aubin P, Zisook M, Stirling L, Wood R J and Walsh C J 2013 Soft wearable motion sensing suit for lower limb biomechanics measurements *Proc. IEEE Int. Conf. on Robotics and Automation (Karlsruhe, Germany)* pp 5289–96

[35] Shin D, Sardellitti I, Park Y-L, Khatib O and Cutkosky M 2010 Design and control of a bio-inspired human-friendly robot *Int. J. Robot. Res.* **29** 571–84

[36] Jien S, Hirai S, Ogawa Y, Ito M and Honda K 2009 Pressure control valve for Mckibben artificial muscle actuators with miniaturized unconstrained pneumatic on/off valves *Proc. IEEE/ASME Int. Conf. on Advanced Intelligent Mechatronics (Singapore)* pp 1383–8

[37] Kerscher T, Zoellner J M, Dillmann R, Stella A and Caporaletti G 2006 Model and control of joints driven by fluidic muscles with the help of advanced automatic algorithm generation software *Climbing Walking Robots* **4** 245–52

[38] Wolbrecht E T, Leavitt J, Reinkensmeyer D J and Bobrow J E 2006 Control of a pneumatic orthosis for upper extremity stroke rehabilitation *Proc. 28th IEEE EMBS Annual Int. Conf. (New York, NY)* pp 2687–93

[39] Chou C-P and Hannaford B 1996 Measurement and modeling of McKibben pneumatic artificial muscles *IEEE Trans. Robot. Autom.* **12** 90–102

[40] Tondu B and Lopez P 2000 Modeling and control of Mckibben artificial muscle robot actuators *IEEE Control Syst. Mag.* **20** 15–38

[41] Belforte G, Eula G, Appendino S and Sirolli S 2011 Pneumatic interactive gait rehabilitation orthosis: design and preliminary testing *Proc. Inst. Mech. Eng.* H **225** 158–69

[42] Wolbrecht E T, Chan V, Reinkensmeyer D J and Bobrow J E 2008 Optimizing compliant, model-based robotic assistance to promote neurorehabilitation *IEEE Trans. Neural Syst. Rehabil. Eng.* **16** 286–97

[43] Balasubramanian K and Rattan K S 2003 Fuzzy logic control of a pneumatic muscle system using a linearizing control scheme *Proc. 22nd Int. Conf. North American Fuzzy Information Processing Society (Chicago, IL)* pp 432–6

[44] Balasubramanian K and Rattan K S 2005 Trajectory tracking control of a pneumatic muscle system using fuzzy logic *Proc. Annual Meeting North American Fuzzy Information Processing Society (Ann Arbor, MI)* pp 472–7

[45] Thanh T D C and Ahn K K 2006 Nonlinear PID control to improve the control performance of 2 axes pneumatic artificial muscle manipulator using neural network *Mechatronics* **16** 577–87

[46] Bertetto A M and Ruggiu M 2004 Characterization and modeling of air muscles *Mec. Res. Commun.* **31** 185–94

[47] Reynolds D B, Repperger D W, Phillips C A and Bandry G 2003 Modeling the dynamic characteristics of pneumatic muscle *Ann. Biomed. Eng.* **31** 310–7

[48] Au S K, Weber J and Herr H 2007 Biomechanical design of a powered ankle–foot prosthesis *Proc. IEEE 10th Int. Conf. on Rehabilitation Robotics* pp 298–303

[49] Au S K, Weber J and Herr H 2009 Powered ankle–foot prosthesis improves walking metabolic economy *IEEE Trans. Robot.* **25** 51–66

[50] Eilenberg M F, Geyer H and Herr H 2010 Control of a powered ankle-foot prosthesis based on a neuromuscular model *IEEE Trans. Neural Syst. Rehabil. Eng.* **18** 164–73

[51] Cho Y M, Xu G and Kailath T 1994 Fast identification of state-space models via exploitation of displacement structure *IEEE Trans. Autom. Control* **39** 2004–17

[52] Pérez Arancibia N O, Gibson S and Tsao T-C 2004 Adaptive control of MEMS mirrors for beam steering *Proc. ASME Int. Mechanical Engineering Congress and Exposition (Anaheim, CA)* p 60256

[53] Ljung L 1999 *System Identification* (Upper Saddle River, NJ: Prentice-Hall)

[54] Van Overschee P and De Moor B 1996 *Subspace Identification for Linear Systems* (Norwell, MA: Kluwer)

[55] Rose J and Gamble J G 2006 *Human Walking* (Philadelphia, PA: Lippincott Williams & Wilkins)

[56] Dullerud G E and Paganini F 2000 *A Course in Robust Control Theory* (New York: Springer)

[57] Pérez-Arancibia N O, Tsao T-C and Gibson J S 2010 A new method for synthesizing multiple-period adaptive-repetitive controllers and its application to the control of hard disk drives *Automatica* **46** 1186–95

[58] Sacks A, Bodson M and Khosla P 1996 Experimental results of adaptive periodic disturbance cancellation in a high performance magnetic disk drive *ASME J. Dyn. Syst. Meas. Control* **118** 416–24

[59] Connelly D M and Vandervoort A A 2000 Effects of isokinetic strength training on concentric and eccentric torque development in the ankle dorsiflexors of older adults *J. Gerontol. A Biol. Sci. Med. Sci.* **55** B465–72

[60] Fowler E G, Ho T W, Nwigwe A I and Dorey F J 2001 The effect of quadriceps femoris muscle strengthening exercises on spasticity in children with cerebral palsy *Phys. Ther.* **81** 1215–23